# Journal Pre-proof

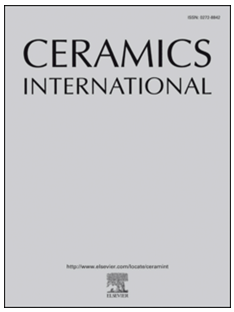


Crystalline structure and phase development in $Zr_xTi_{1-x}O_2$ (x=0.9–0.2) ceramic nanofibers from electrospun precursors (CH-3:L03)

Riley Yager, Sarah Nealy, Rachel Day, Courtney Severino, Andrei Stanishevsky

PII: S0272-8842(22)03606-9

DOI: https://doi.org/10.1016/j.ceramint.2022.10.025

Reference: CERI 34461

To appear in: *Ceramics International*

Received Date: 29 August 2022

Revised Date: 18 September 2022

Accepted Date: 3 October 2022

Please cite this article as: R. Yager, S. Nealy, R. Day, C. Severino, A. Stanishevsky, Crystalline structure and phase development in $Zr_xTi_{1-x}O_2$ (x=0.9–0.2) ceramic nanofibers from electrospun precursors (CH-3:L03), *Ceramics International* (2022), doi: https://doi.org/10.1016/j.ceramint.2022.10.025.

CERI-D-22-09746
*Revised manuscript – Clean version*

# Crystalline Structure and Phase Development in $Zr_xTi_{1-x}O_2$ (x=0.9–0.2) Ceramic Nanofibers from Electrospun Precursors (CH-3:L03)

Riley Yager, Sarah Nealy, Rachel Day, Courtney Severino, Andrei Stanishevsky

*Department of Physics, University of Alabama in Birmingham, Birmingham, Alabama 35294 USA*

*Corresponding Author:*

*Riley Yager*
*Tel: (448)201-3395*
*E-mail: ryager7@uab.edu*

*University of Alabama at Birmingham,*
*Department of Physics,*
*310 Campbell Hall*
*1300 University Boulevard,*
*Birmingham, AL 35233, USA*

# Crystalline Structure and Phase Development in $Zr_xTi_{1-x}O_2$ (x=0.9–0.2) Ceramic Nanofibers from Electrospun Precursors (CH-3:L03)

Riley Yager*, Sarah Nealy, Rachel Day, Courtney Severino, Andrei Stanishevsky

*Department of Physics, University of Alabama in Birmingham, Birmingham, Alabama 35294 USA*

## Abstract

Nanofibrous $Zr_xTi_{1-x}O_2$ (x=0.9–0.2) ceramic materials were produced using a high-yield, free surface alternating field electrospinning (AFES) process (a.k.a. AC-electrospinning) from metal alkoxide precursor solutions. Depending on the precursor composition, the production rates of 4.8–6.4 g/h in terms of the resulting ceramic nanofibers were demonstrated with a single-electrode AFES system. The average diameter of $Zr_xTi_{1-x}O_2$ fibers varied in the range of 190–435 nm, depending on the alkoxide/polymer mass ratio in the precursor and annealing temperature. Zr/Ti molar ratio is a key factor that determines the crystallization temperature and phase composition of $Zr_xTi_{1-x}O_2$ nanofibers after thermal processing between 600 and 1200°C, but it has a moderate effect on textural properties of the resulting nanofibers. When the molar fraction of zirconia is >0.7, the nanofibers are composed primarily of a nanocrystalline titania-rich $TiO_2$-$ZrO_2$ solid solution without the formation of separate $TiO_2$ phase. At zirconia molar fraction of 0.5, stable orthorhombic $Zr_{0.5}Ti_{0.5}O_2$ zirconium titanate structure forms above 680 °C. $TiO_2$ (anatase or rutile) forms as a separate phase in addition to $Zr_xTi_{1-x}O_2$ phases when Zr molar fraction is 0.2, depending on the annealing temperature. The results of this study demonstrate that a large variety of nanofibrous $ZrO_2$-$TiO_2$ ceramic materials with tailored compositions can be efficiently prepared for targeted applications by using free-surface AFES and appropriate thermal processing.

**Keywords:** AC-electrospinning, $ZrO_2$, $TiO_2$, ceramic, nanofibers, zirconium titanate

## 1. INTRODUCTION

Transition metal oxides in the $ZrO_2$–$TiO_2$ system are of high technological interest due their ability to form a variety of crystalline phases, which provide useful combinations of properties for many demanding applications [1-5]. For example, $TiO_2$–$ZrO_2$ mixed oxides receive much attention as catalysts and catalyst supports [2], sensors [3], filtration membranes [4], thermal insulators [5] with high thermal shock resistance, and many other. For such applications, the nanoscale grain sizes, large surface area and porosity, thermal stability and mechanical integrity in harsh environments are critical parameters of the material [6].

Nanocrystallinity, large surface area and micro-/meso-porosity of $ZrO_2$ and $TiO_2$ materials is achievable by appropriate fabrication techniques. Sol-gel synthesis is one of the most common methods in fabrication of $ZrO_2$, $TiO_2$, and $ZrO_2$–$TiO_2$ mixed oxide nanosized powders [7,8]. However, the consolidation of loose nanosized powders into the practical structures frequently leads to significant loss of their nanosize-enabled functionality due to the growth of crystallites, pore size and surface area reduction [9].

Fabrication of $ZrO_2$–$TiO_2$ materials in the form of one-dimensional (1-D) entities such as nanofibers brings many advantages to the material handling and processing. Nanofibers in $ZrO_2$–$TiO_2$ system have been mainly prepared using different spinning methods including centrifugal [10,11], gas jet [12], and direct current (DC) electrospinning techniques [13,14]. DC electrospinning has been the most common method so far. Both $TiO_2$ and $ZrO_2$ binary oxide nanofibers, extended nanofibrous meshes, and bulk three-dimensional (3-D) nanofibrous shapes have been prepared and demonstrated good mechanical properties, flexibility and resilience along with their enhanced functionality when compared to nanopowders [15-17]. However, there are not many reports on the fabrication of mixed $ZrO_2$–$TiO_2$ and $Zr_xTi_{1-x}O_2$ nanofibers with various Zr/Ti

molar ratios [18-23], and the most studies on $Zr_xTi_{1-x}O_2$ nanofibers are limited to relatively low, up to 600 ºC, processing temperatures. For example, Dong et al [18] prepared heat-resistant $ZrO_2/TiO_2$ core/shell nanofibrous sponges using a coaxial capillary DC electrospinning. They found that the crystallized fibers are composed of a tetragonal $ZrO_2$ core and anatase $TiO_2$ shell, which converts to rutile after the annealing at 900 ºC. Such $ZrO_2/TiO_2$ nanofibrous sponges have been stable up to 1200 ºC and exhibited good thermal shock resistance, high resilience, and high near-infrared reflectance, which makes them attractive for high-temperature thermal insulation materials. Su et al [19] prepared $ZrO_2$–$TiO_2$ mixed oxide nanofibers by simultaneous DC electrospinning of $TiO_2$ and $ZrO_2$ precursors from two capillary spinnerets, and demonstrated their good performance as humidity sensors.

$Zr_xTi_{1-x}O_2$ nanofibrous meshes with different Zr/Ti molar ratios have been reported by several research groups [20-23]. Yasin et al [20] found that the DC electrospun $Zr_xTi_{1-x}O_2$ nanofibers annealed at 600 ºC are composed of a mixture of tetragonal $ZrO_2$+$Zr_{0.5}Ti_{0.5}O_2$ at 3.0:1.0, $Zr_{0.5}Ti_{0.5}O_2$ only at 1.0:1.0, and anatase $TiO_2$+$Zr_{0.5}Ti_{0.5}O_2$ phases at 1.0:3.0 Zr/Ti molar ratios. The formation of a single phase $Zr_{0.5}Ti_{0.5}O_2$ at Zr/Ti 1.0:1.0 molar ratio has also been observed by Yu et al [21] in dry-spun microfibers. The authors also determined that after annealing at 500 ºC the fibers with Zr/Ti molar ratio <0.7:0.3 remain amorphous, whereas a mixed phase tetragonal/monoclinic $ZrO_2$ forms in the fibers with Zr/Ti molar ratio of 0.8:0.2. Song et al [22] found the DC electrospun and annealed at 600 ºC $Zr_xTi_{1-x}O_2$ nanofibers become less brittle when the molar fraction of zirconia increases from 0 to 0.2. The fibers were composed of only anatase $TiO_2$ phase even at 20 mol% of Zr in that study. Barakat et al [23] reported $Zr_xTi_{1-x}O_2$ nanofibrous meshes with x = 0, 0.25, 0.5, 0.75, and 1.0 prepared by <600 ºC thermal processing of DC electrospun precursor fibers based on metal alkoxide and polyvinyl acetate polymer. The

nanofibers with 0.75 $ZrO_2$ molar fraction showed the best catalytic activity toward lignin liquefaction. There are no reports on the crystalline phase and surface morphology evolution in $Zr_xTi_{1-x}O_2$ nanofibers in a broader range of temperatures, especially above 600 ºC, and whether such nanofibers can be produced in sizeable and scalable quantities.

In present work, $Zr_xTi_{1-x}O_2$ (x=0.9–0.2) nanofibers have been fabricated by using an uncommon, high-yield free-surface alternating field electrospinning (AFES) process (a.k.a. AC-electrospinning) [24]. The method is based on the generation of the propagating liquid precursor jets by applying 12–40 kV rms AC-voltage to usually a dish-shaped electrode with a diameter up to several centimeters. The propagating jets develop into dense fibrous flows where the propagating fibers carry almost no electric charge. The fibrous flows are carried away by "electric wind" [25], a key phenomenon in AC-electrospinning. Due to relatively slow motion of the fibrous flow (0.2–1.8 m/s) and low residual electric charge of the moving fibers, AFES processing significantly simplifies the precursor fibers collection and handling [26]. AFES has been shown to efficiently generate polymer [27–30] and inorganic, including $ZrO_2$ and $TiO_2$ [31–34] nanofibers with the precursor solution feeding rates up to 1200 ml/h [24,35].

The goal of this study has been to explore the potential of AFES for sizeable production of $Zr_xTi_{1-x}O_2$ ternary oxide nanofibers using metal alkoxide precursors, and establish the precursor-process-structure relationships for controlled synthesis of nanofibrous $Zr_xTi_{1-x}O_2$ with desired microstructure and phase composition. Trends in nanofiber generation during AFES and their crystallization behavior in the range of annealing temperatures from 600 to 1200 ºC have been observed and analyzed.

## 2. EXPERIMENTAL METHODS

### 2.1. Precursor Materials and Preparation

Titanium(IV) n-Butoxide ($Ti(OBu)_4$, 99+%), Zirconium propoxide ($Zr(OPr)_4$, 70 wt% in 1-propanol), polyvinylpyrrolidone (PVP, $M_w$=1,300,000), hydroxypropyl cellulose (HPC, $M_w$=100,000), glacial acetic acid (AA, Reagent grade) and acetylacetone (2,4-pentanedione, 99%) supplied by Alfa Aesar, and ethanol (200 Proof, Decon Labs, Inc) were used to prepare the $Zr_xTi_{1-x}O_2$ (x=0.9–0.2) precursor solutions. In a typical procedure, the titanium and zirconium alkoxides were combined with a mixture of ethanol, acetic acid and acetylacetone in a dry box, and this precursor component was added to the 10 wt% solution of PVP/HPC (1.0/1.0 mass ratio) polymer blend in ethanol. The molar ratio of alkoxide to acetic acid was maintained as 1.0/1.0 in all experiments. The amount of acetylacetone varied from 0.5 to 5.0 wt% of total weight of the precursor with the increase of zirconium propoxide component. The amount of solvent in each precursor was adjusted to maintain ~5 wt% polymer concentration. The alkoxide to polymer mass ratio was set to yield ~1.5 g of ceramic material per one gram of polymer carrier. The precursors were stirred for up to 24 h using a magnetic stirrer and kept in sealed HDPE bottles at normal laboratory conditions. All precursor compositions were stable for at least six month when stored in sealed bottles under normal laboratory conditions.

### 2.2. Fabrication of $Zr_xTi_{1-x}O_2$ nanofibers

The generation of $Zr_xTi_{1-x}O_2$ (x=0.9–0.2) precursor nanofibers was done by using AFES process operated at 12–40 kV rms AC voltage (60 Hz frequency) [33,34]. The precursor solution was fed to a metal dish electrode with a diameter of 25 mm through an electrically insulated fluid

line, which could deliver the fluid at the rates up to 10 mL/min. The fibers were collected either on a rotating cylindrical (40–240 rpm, 10–30 cm diameter) or on a stationary flat plastic mesh collectors placed above the electrode. The shortest distance between the electrode and collector surface was 20 cm.

Usually, 60–100 mL of precursor was used in each experiment. The collected fibers were placed in a programmable furnace (Isotemp, Fisher Scientific), heated at 1.5–2.5 ºC/min rate, held at 600–1200 ºC for 3 hours, and then cooled naturally.

2.3. Characterization

Apparent viscosity of precursor solutions was measured by using a HAAKE RotoVisco 1 viscometer (Thermo Scientific) in a parallel plate configuration at steady shear rate of 1000 rpm over a period of 120-seconds. The electrical conductivity of the precursor solutions was determined with a FP30 conductivity meter (Mettler Toledo).

Decomposition of the precursor fibrous material was analyzed by using Thermal Gravimetric Analysis (TGA, TG/DTA-SETSYS-16/18 instrument, SETARAM, France) in synthetic air in the range of 20–1000 ºC at the heating rate of 10 ºC/min. Thermogravimetric (TG), differential thermal analysis (DTA), and differential thermogravimetric (DTG) curves were recorded simultaneously. The TGA instrument was coupled through a heated capillary adapter to a quadrupole mass spectrometer (QMS-422 ThermoStar from Balzers Instruments, 100 amu, 70 eV electron impact ionization) to monitor principal volatile species produced during the pyrolysis of precursor fibers. Ion mass spectroscopy (MS) data sets were processed using the Quadstar 422 software.

The diameter, surface morphology and elemental composition of annealed $Zr_xTi_{1-x}O_2$ nanofibers were analyzed by scanning electron microscopy (SEM/EDS, FEI Quanta 650 FE-SEM) equipped with an Oxford X-max 80 SDD EDS detector. A few nanometers thick, AuPd layer was sputter coated onto the samples to reduce electric charging during the imaging. SEM imaging was performed in secondary electron mode at an accelerating voltage of 15 kV and electron probe current 2.5 μA. The EDS elemental composition and Zr/Ti mol% ratio was averaged over at least five 100×100 $\mu m^2$ areas. ImageJ image processing program was used to determine the fiber diameters and their size distribution. At least three SEM images of different areas of the sample with up to 250 fibers total were used to obtain the average fiber diameter in each sample.

Crystalline phase analysis was performed using X-ray diffraction (XRD) to investigate phase composition and crystallite size for each nanofiber composition and annealing temperature. The XRD patterns were acquired using a PANalytical Empyrean X-ray diffractometer (Copper $K_{\alpha 1}$ radiation, λ=1.54059 Å, 45 kV/40 mA). The patterns were acquired in the range of 10–90 degrees 2θ in a continuous scan mode with 0.01313° step size. The diffraction optics included a hybrid monochromator with a 1/8° divergence and a 1/16° anti-scattering slits, and a parallel plate collimator on the diffracted beam path with a PIXcel$^{1D}$ detector. Crushed nanofiber samples were rotated during the measurements to reduce the effect of preferred orientation in the crystalline phase. Phase composition and crystallite size analyses were performed using the PANalytical High Score Plus software package and the International Centre for Diffraction Data (ICDD) powder diffraction file (PDF-2 ver. 2013) database. The strongest XRD peaks (up to three, where possible) of each distinguishable crystalline phase were used to determine the average crystallite size.

## RESULTS AND DISCUSSION

All prepared precursors were stable for at least six months and demonstrated reproducible spinnability in AFES process during that entire time interval. The best precursor spinnability and fiber flow stability were achieved at 28–30 kV rms AC voltage (60 Hz frequency). The precursor fibers were collected at a rate between 7.5 and 11.0 g/h, depending on the precursor composition. Table 1 summarizes the precursor compositions, viscosities, electrical conductivity, and the flow rates along with the process productivity in terms of the resulting nanofibrous ceramic material. The achieved production rates in Table 1 correspond to 4.8–6.4 g/h in terms of the resulting $Zr_xTi_{1-x}O_2$ nanofibrous ceramic material. Those rates are comparable to 5.2 g/h AFES productivity of pure $TiO_2$ nanofibers [34], and noticeably higher than 1.5 g/h productivity reported for AFES $ZrO_2$ nanofibers [33]. It should be noted that the different precursor composition based on zirconyl chloride was used in a latter case. The Ti and Zr alkoxides were used in the present study because of the precursors were more stable and chlorine-free. The precursor viscosity and electrical conductivity are the main factors that determines the spinnability in free-surface AFES process. A large change in electrical conductivity of the precursor (Table 1) can be mainly associated with the concentration of acetylacetone (AcAc) as the stabilizing agent in the precursor. Acetylacetone decomposes by alcoholysis reaction and yields acetone and ester of the reacting alcohol or diol [36,37]. The substitution of propoxide on the $Zr(acac)_4$ complex is much faster than that of the $Ti(acac)_4$ complex because propoxide decomposes to an intermediate n-propyl acetate ligand, and differences in the amount of AcAc incorporated depend on the alkoxide precursor composition, and particularly the presence of $Zr(acac)_4$ complexes in the solution. This also determines the composition of the formed Zr and Ti intermediates, which contributes to the electrical conductivity of Zr/Ti alkoxide mixed precursor. It appears that the precursor viscosity in the range of 100–130

mPa·s resulted in the best process performance, whereas lower viscosities led to intermittent fiber generation and higher viscosities restricted the liquid jet generation and fiber clamping inside the flow. The precursor flow take-off rate was in the range of 1.10–1.55 mL/min with 25 mm electrode diameter (Table 1). The flow rate increases with the decrease of Zr/Ti molar ratio and electrical conductivity of the precursor. On the one hand, according to the electrohydrodynamic (EHD) flow models in electrospinning [38], the decrease of the electrical conductivity is responsible for the increased strength of electric field and a greater Coulomb force in the precursor layer. On the other hand, decrease in Zr/Ti molar ratio leads to only a small decrease in the amount of fiber mass produced per milliliter of the precursor. Thus, similarly to a case of AFES of pure $TiO_2$ nanofibers reported by Nealy et al [34], electrical conductivity of $Zr_xTi_{1-x}O_2$ precursor is the key factor that affects the flow take off rate and determines the process productivity in AFES.

TGA results show that all collected precursor fibers lost about 47±4% of their mass after the thermal processing at 600 ºC (Fig.1a). The main loss of the mass occurs between 300 and 500 ºC due to the exothermic decomposition of the polymeric fraction and Zr/Ti intermediates (Fig.1b,c). The TGA/MS signals plateaued between 500 and 600 ºC. There was no further mass change observed in $Zr_xTi_{1-x}O_2$ nanofibers with Zr/Ti molar ratio of 0.2:0.8 after the annealing at up to 1000 ºC. Small exothermic peaks in TGA signals of $Zr_xTi_{1-x}O_2$ nanofibers with 0.5:0.5 and 0.7:0.3 Zr/Ti molar ratios in the range of 650–720 ºC indicate fast crystallization of the material with simultaneous additional ~3 % mass loss (Fig.1b). This additional mass loss is associated with the removal of carbon residue, which is confirmed by the corresponding peaks in ion emission signal (Fig.1c). An increase in C, $CO_2$, and $HCO_2$ positive ion emission between 800 and 1000 ºC can be related to the elimination of trace carbon still present in the micro/meso-pores because of their progressing diffusion and coalescence during the grain growth in the fibers. The nanofibers with

0.9:0.1 Zr/Ti molar ratio also showed gradual, ~2% mass loss due to the carbon residue removal in the range of 600–800 ºC, which was similar to undoped $ZrO_2$ nanofibers [34].

SEM analysis of $Zr_xTi_{1-x}O_2$ nanofibers annealed at 600 ºC revealed randomly packed nanofibrous assemblies (Fig.2a-d). The fiber diameters varied from 220±56 to 290±123 nm after the annealing at that temperature, depending on the alkoxide/polymer ratio in the precursor (Fig.3). The average diameters of $Zr_xTi_{1-x}O_2$ nanofibers derived from AFES precursors are within the range of typical fiber diameters reported for DC-electrospun fibers in $ZrO_2$-$TiO_2$ system [12-23]. Thinner, sub-100 nm, $Zr_xTi_{1-x}O_2$ nanofibers can be possible in AFES by either reducing the alkoxide/polymer mass ratio at the expense of the final product yield [33], or by the optimization of the precursor to maintain its spinnability at lower concentration of the polymer fraction but the same content of alkoxides. The Zr/Ti molar ratio in ceramic nanofibers after the annealing between 600 and 1200 ºC was close to the ratio preset in the precursor according to EDS data (Fig.2e-h). A small deviation between the preset and measured composition has been associated with the preparation routine of relatively small precursor quantities and the precision of EDS analysis.

$Zr_xTi_{1-x}O_2$ nanofibers with all tested compositions had smooth and featureless surface morphology after the annealing at 600 ºC. However, there are clear trends in the surface morphology changes depending on Zr/Ti molar ratio after the annealing at higher temperatures. SEM images of $Zr_xTi_{1-x}O_2$ nanofibers annealed at 800 ºC (Fig.4a-d) indicate the development of more grainy structure when Zr/Ti molar ratio decreases, but the fibers remain relatively smooth. The fiber diameter was found to decrease after the annealing at 800 ºC, and the average fiber diameters were between 190±55 and 260±115 nm, depending on the precursor composition, due to the progressing fiber crystallization and densification (Fig.3). After the annealing at 1000 ºC, the fibers became progressively rougher and more macroporous with the decreasing Zr/Ti molar

ratio (Fig. 4e-h). Well-defined grain structure of $Zr_xTi_{1-x}O_2$ nanofibers develops after the annealing at 1200 ºC, especially in the fibers with minimum and maximum Zr/Ti molar ratios (0.2:0.8 and 0.9:0.1, respectively) (Fig.4i-l). When compared to 800 ºC annealed nanofibers, the average fiber diameter increased from the smallest observed (190 nm, 0.7:0.3 Zr/Ti molar ratio) to 285±65 nm, and from the largest (260 nm, 0.2:0.8 Zr/Ti molar ratio) to 435±118 nm (Fig.3) after the annealing at 1200 ºC due the continuing grain growth, axial shrinkage, and interfiber fusion. The interfiber fusion can increase the fiber diameter when a long segment of bundled, parallel nanofibers forms a single fiber due to sintering. This is a contributing but not the major process that led to the fiber diameter increase in the present study, where the relatively little fiber bundling was observed. Conversely, the grain growth in the polycrystalline $Zr_xTi_{1-x}O_2$ nanofibers had a dominating effect. When temperature increases, the growth of larger grains, probably composed of several misaligned crystallites, was observed (Fig.4i-l). The fiber diameter restricts the grain growth in radial direction, and causes the grain to consume the material along the fiber to attain the equilibrium morphology [39,40]. As the result, the fibers contract axially which leads to further increase of the grain size, changes of the grain shape, and a larger fiber diameter. This process was the most pronounced in $Zr_xTi_{1-x}O_2$ nanofibers with Zr/Ti molar ratio of 0.2:0.8, which reveal the largest grain size after the annealing at 1200 ºC (Fig.4l). Although the integrity of all tested $Zr_xTi_{1-x}O_2$ nanofibers was mostly preserved after the annealing at 1200 ºC despite the partial sintering, fusion and/or breakage of individual nanofibers due to the fiber axial shrinkage, the fibrous assemblies become more brittle.

According to XRD data for $Zr_xTi_{1-x}O_2$ nanofibers with Zr/Ti molar ratio of 0.9:0.1 (Fig.5a), the material calcined at 600°C for 3 h crystallizes in the form of a $ZrO_2$-$TiO_2$ solid solution with primarily tetragonal $ZrO_2$ phase (PDF #00-014-0534, mean crystallite size of 13.5 nm) and traces

of monoclinic phase of $ZrO_2$ (*m*-$ZrO_2$). It should be noted that the crystallization of Zr/Ti = 0.9:0.1 nanofibrous material already starts at > 400 ºC. The initial formation of metastable tetragonal phase of $ZrO_2$ (*t*-$ZrO_2$) is associated with the spontaneous nucleation of very small (<10 nm) zirconia crystallites with high surface energy. This phase is stabilized by the small size of crystallites, presence of oxygen vacancies, and carbon residue from the decomposing polymer matrix [41]. Tetragonal phase gradually converts to monoclinic phase with the increasing temperature with the both phases having less than 20 nm average crystallite size after the annealing up to 1000 ºC for 3 h (Fig.6a). The presence of titania had a small effect on the stability of the initially formed tetragonal phase in nanofibers with Zr/Ti ratio of 0.9:0.1 at elevated temperatures when compared to pure $ZrO_2$ [33]. The crystallite size increases rapidly at higher annealing temperatures, and the fibrous material is represented by a single monoclinic phase of $ZrO_2$ (PDF #00-037-1484) with ~48 nm average crystallite size after partial sintering at 1200 ºC for 3 h (Fig.5a, Fig.6a). The calculated average crystallite size is smaller than the apparent 100–500 nm grain size observed in SEM images. However, the larger grains can still consist of several clustered crystallites and have some level of residual stress that results in the XRD peak broadening, which contributes to the calculated crystallite size.

An increase of the fraction of titania in $Zr_xTi_{1-x}O_2$ nanofibers up to Zr/Ti molar ratio of 0.7:0.3 (Fig.5b) leads to a similar result after the annealing at 600 ºC as for material with Zr/Ti molar ratio of 0.9:0.1 (Fig.5a). It has been noted that the crystallization in this case starts spontaneously at 570–590 ºC, depending on the precursor age. No trace of *m*-$ZrO_2$ phase and no formation of $TiO_2$ secondary phases were observed. However, the diffraction pattern of this titania-rich *t*-$ZrO_2$ phase differs a little from that of $Zr_{0.9}Ti_{0.1}O_2$ sample and does not fully match the standard patterns for *t*-$ZrO_2$. The measured composition of this nanofibrous material ($Zr_{0.707}Ti_{0.293}O_2$ according to EDS)

is close to $Zr_3TiO_8$ compound proposed by Troitzsch et al [42]. The strongest peaks (112), (004), (024), (116) and (312) in XRD pattern of the tetragonal $Zr_3TiO_8$ phase match the observed peaks at 30.3, 34.2, 50.3, 58.9 and 60.7° 2θ in $Zr_{0.707}Ti_{0.293}O_2$ nanofibers, but they also partially overlap with the peaks of *t*-$ZrO_2$ phase.

The tetragonal phase with EDS determined composition of $Zr_{0.707}Ti_{0.293}O_2$ remains stable after the annealing at 1000 °C for 3 h. The average crystallite size in $Zr_{0.707}Ti_{0.293}O_2$ nanofibers gradually increases from 9.1 nm at 600°C to 14.7 nm at 800°C and to 17.8 nm after the annealing at 1000°C (Fig.6a). The relative intensity of XRD peaks that were assigned to $Zr_3TiO_8$ phase increased after the annealing at 800 and 1000 °C. Although the $Zr_{0.707}Ti_{0.293}O_2$ nanofibers were already crystalline after the annealing at 600 °C, DTA reveals a sharp exothermic peak due to the crystallization at ~670 °C (Fig.1b). This indicates that the fiber structure can represented by two co-existing crystalline phases (titania-rich *t*-$ZrO_2$ solid solution and $Zr_3TiO_8$) above that temperature. Further annealing of $Zr_xTi_{1-x}O_2$ nanofibers with Zr/Ti molar ratio of 0.7:0.3 at 1200°C leads to the formation of a mixture of the titania-rich tetragonal (minor, perhaps as $Zr_3TiO_8$) and monoclinic (major) $ZrO_2$ phases with the average crystallite sizes of 21.7 nm and 27.3 nm, respectively (Fig.6a). There was no sign of the formation of $TiO_2$ crystalline phases or stoichiometric $Zr_{0.5}Ti_{0.5}O_2$ compound as reported, for example, by Verma et al [43]. Literature data indicate that the solubility of $TiO_2$ in $ZrO_2$ can be up to 13–16 mol% [44] at the temperatures up to 1500 °C and the metastable solid solution with monoclinic $ZrO_2$ structure forms without a change in the material composition on cooling to room temperature. Such solubility is smaller than the apparent 29 mol% $TiO_2$ solubility seen in $Zr_xTi_{1-x}O_2$ nanofibers. Similar solubility levels have been reported only in high-temperature high-pressure studies of $TiO_2$-$ZrO_2$ system and the resulting phases depended on the cooling rate of the system [42]. It is possible that the formation of mixed phase

structure in $Zr_{0.707}Ti_{0.293}O_2$ nanofibers (titania-rich *t*-$ZrO_2$ and $Zr_3TiO_8$) between 600 and 1000 ºC is promoted by a small crystallite size and the presence of oxygen vacancies and other defects. It can lead to a high hydrodynamic stress in the system, which substitutes for static high pressure and provide the conditions for up to 29 mol% of $TiO_2$ to remain dissolved in the structure. Similarly, AFES derived $Zr_{0.707}Ti_{0.293}O_2$ nanofibers may be a mixture of primarily titania-rich *m*-$ZrO_2$ solid solution and residual *t*-$ZrO_2$ and/or $Zr_3TiO_8$ phases after the annealing at 1200 ºC and naturally cooled down at relatively high rate.

The structure of $Zr_xTi_{1-x}O_2$ nanofibers with Zr/Ti molar ratio of 0.5:0.5 is mainly X-ray amorphous after the annealing at 600 ºC (Fig.5c). A small peak at 30.2º 2θ in 600 ºC pattern is associated with the formation of *t*-$ZrO_2$ phase due to imperfect stoichiometry of the $Zr_{0.5}Ti_{0.5}O_2$ sample (actual composition $Zr_{0.508}Ti_{0.492}O_2$ according to EDS). Nanofibrous $Zr_{0.5}Ti_{0.5}O_2$ material is fully crystallized as zirconium titanate (PDF #01-074-9433) at 800 ºC with the average crystallite size of ~15.3 nm. According to TGA analysis of this sample, the spontaneous crystallization of zirconium titanate phase occurs at 680 ºC with the simultaneous ~3% mass loss due to the release of carbonaceous residue (Fig.1b). This is within the range of crystallization temperatures (450–750 ºC) of $Zr_{0.5}Ti_{0.5}O_2$ from various precursors and in different processes [45–49]. This phase remains stable and nanocrystalline after the annealing at 1000 and 1200 ºC for 3 h, with the average crystallite size reaching 17.1 and 33.3 nm, respectively (Fig.6b). The minor *t*-$ZrO_2$ impurity phase converts to *m*-$ZrO_2$ (average crystallite size 23.1 nm) as revealed by small peaks at 28.4 and 31.4º 2θ in 1200 ºC XRD pattern.

XRD patterns of $Zr_xTi_{1-x}O_2$ nanofibers with Zr/Ti molar ratio of 0.2:0.8 reveal the crystallization of at least two phases already after the annealing at 600 ºC for 3 h (Fig.5d). One strong peak at 24.8º 2θ is due to anatase $TiO_2$ (*a*-$TiO_2$) phase (PDF #01-070-8501), whereas

another strong peak at 30.9º 2θ has been ascribed to a $Zr_{0.33}Ti_{0.67}O_2$ (PDF #98-003-1311) ternary phase. Anatase $TiO_2$ phase has ~20.1 nm average crystallite size after the annealing at 600°C and it remains stable up to 800 ºC reaching only 21.8 nm crystallite size after the annealing at that temperature (Fig.6c). The phase composition has been estimated as ~40-42 mol% a-$TiO_2$ and 58–60 mol% $Zr_{0.33}Ti_{0.67}O_2$. Rutile $TiO_2$ (*r*-$TiO_2$) phase start to form at 800 ºC (PDF #01-070-7347) and after the annealing at 1000 ºC $TiO_2$ is present only as rutile (~48.1 nm crystallite size). Interestingly, the crystallite size of $Zr_{0.33}Ti0_{.67}O_2$ phase gradually reduces from 14 nm after the annealing at 600 °C to 13.2 nm at 800°C and then to 11 nm at 1000 °C (Fig.6c). The decrease in the crystallite size of $Zr_xTi_{1-x}O_2$ phase can actually be due the initial $Zr_{0.33}Ti0_{.67}O_2$ phase decomposition and nucleation of another phase between 800 and 1000 ºC. After the annealing at 1200 ºC the XRD pattern of the ternary phase in nanofibers with 0.2:0.8 Zr/Ti molar ratio matches the $Zr_{0.45}Ti_{0.55}O_2$ phase (PDF #01-074-9433). The phase composition of nanofibers in this case becomes ~54 mol% *r*-$TiO_2$ and ~46 mol% $Zr_{0.45}Ti_{0.55}O_2$. The observed behavior suggests that *r*-$TiO_2$ and $Zr_{0.45}Ti_{0.55}O_2$ are more stable phases than the initially formed $Zr_{0.33}Ti_{0.67}O_2$. These results significantly differ from the data reported elsewhere for $Zr_xTi_{1-x}O_2$ materials with similar composition. For example, Sham et al [50] found that $Zr_{0.22}Ti_{0.78}O_2$ prepared by a sol-gel process are composed of *r*-$TiO_2$ (64.3 mol%), $Zr_5Ti_7O_{24}$ (24.4 mol%) and *t*-$ZrO_2$ (11.3 mol%) after the annealing at 1000 ºC. In another study, Lv et al [51] observed a single, nanocrystalline (average size of crystallites ~19.7 nm) *a*-$TiO_2$ phase in $Zr_{0.2}Ti_{0.8}O_2$ nanofibers prepared by DC electrospinning from Zr and Ti alkoxide precursors and annealed at 600 ºC. Such variations in the phase composition can be related to the specific chemical composition of precursors and thermal treatment protocols.

## CONCLUSIONS

An uncommon, high-yield free surface alternating field electrospinning process has been successfully utilized to efficiently produce nanofibrous ceramic materials within $ZrO_2$-$TiO_2$ system from precursor solutions based on various molar ratios of titanium and zirconium alkoxides. The capability of a single electrode AFES-based process to produce between 4.8 and 6.4 g/h of the material in terms of the resulting ceramic nanofibers with the average diameters from 190 to 435 nm, depending on the precursor composition and annealing temperature, has been demonstrated. The AFES process productivity has been found to depend strongly on the electrical conductivity and molar ratio of titanium and zirconium alkoxides in the precursor solution.

Chemical composition of the $Zr_xTi_{1-x}O_2$ precursors had only a moderate effect on textural properties of the resulting ceramic nanofibers, but it has been crucial to determining phase composition of the materials after thermal processing in air between 600 and 1200°C. In general, the formed crystalline phases, their stability and transformations are determined by the diffusion controlled atomic scale interaction of the precursor components, presence of carbonaceous residue during the decomposition of polymer fraction, and the nanoscale size, surface energy and defect states of the initially formed crystallites.

The formation of single-phase nanocrystalline zirconia nanofibers has been observed with Zr/Ti molar ratio of 0.9:0.1. The formation of nanofibers composed of a mixed titania-rich $TiO_2$-$ZrO_2$ solid solution and possibly $Zr_3TiO_8$ phase has been suggested at Zr/Ti molar ratio of 0.7:0.3.

Nanofibers with $Zr_{0.5}Ti_{0.5}O_2$ zirconium titanate structure form from the precursors with 0.5:0.5 Zr/Ti molar ratio. This zirconium titanate phase starts to crystallize above 680 °C and is stable during sintering at 1200 °C for 3 h.

At least two distinct phases form simultaneously at 600 ºC in $Zr_xTi_{1-x}O_2$ nanofibers with Zr/Ti molar ratio of 0.2:0.8, namely anatase $TiO_2$ and $Zr_{0.33}Ti_{0.67}O_2$ phase. The latter phase has been found unstable and it gradually converted to more zirconia-rich phase resulting in a two-phase nanocrystalline fibers composed of rutile $TiO_2$ and $Zr_{0.45}Ti_{0.55}O_2$ phases at higher annealing temperatures.

The results of this study demonstrate that by varying Zr/Ti molar ratio in the precursor a large variety of nanofibrous ceramic materials within $ZrO_2$-$TiO_2$ system with tailored compositions and textural properties for targeted applications can be efficiently prepared by using high-yield AFES and appropriate thermal processing protocols.



## ACKNOWLEDGEMENTS

This work has been primarily supported by the National Science Foundation (NSF) [Grant number DMR-1708600]. RY, SN, RD and CS thank the support from the NSF International Research Experience for Students (IRES) Program [Grant number OISE-1558268]. The authors thank Mr. Micah Armstrong for EDS and Dr. Karolina Chalupka for TGA data acquisition.

## REFERENCES

1. T. Yamaguchi, Application of $ZrO_2$ as a catalyst and a catalyst support, Catal. Today 20 (1994) 199–217. https://doi.org/10.1016/0920-5861(94)80003-0
2. B. M. Reddy, A. Khan, Recent advances on $TiO_2$-$ZrO_2$ mixed oxides as catalysts and catalyst supports, Catal. Rev. Sci. Eng. 47 (2005) 257–296. http://doi.org/10.1081/CR-200057488
3. S.-L. Yang, J., -M. Wu, $ZrO_2$-$TiO_2$ ceramic humidity sensors, J. Mater. Sci. 26 (1991) 631–636. http://doi.org/10.1007/BF00588297

4. Y. Lu, T. Chen, X. Chen, M. Qiu, Y. Fan, Fabrication of $TiO_2$-doped $ZrO_2$ nanofiltration membranes by using a modified colloidal sol-gel process and its application in simulative radioactive effluent, J. Membr. Sci. 514 (2016) 476–486. http://doi.org/10.1016/j.memsci.2016.04.074
5. E. Lopez-Lopez, C. Baudin, R. Moreno, I. Santacruz, L. Leon-Reina, M.A.G. Aranda, Structural characterization of bulk $ZrTiO_4$ and its potential for thermal shock applications, J. Eur. Ceram. Soc. 32 (2012) 299–306. http://doi.org/10.1016/j.jeurceramsoc.2011.08.004
6. S. Bhaskar, J.G. Park, K.S. Lee, S.Y. Kim, I.J. Kim, Thermal and mechanical behavior of $ZrTiO_4$-$TiO_2$ porous ceramics by direct foaming, Ceram. Int. 42 (2016) 14395–14402. http://doi.org/10.1016/j.ceramint.2016.06.019
7. R. Pérez-Hernández, D. Mendoza-Anaya, M. E. Fernández, A. Gomez-Cortés, Synthesis of mixed $ZrO_2$-$TiO_2$ oxides by sol-gel: Microstructural characterization and infrared spectroscopy studies of NOx, J. Mol. Catal. 281 (2008) 200–206. http://doi.org/10.1016/j.molcata.2007.11.008
8. B. Neppolian, Q. Wang, H. Yamashita, H. Choi, Synthesis and characterization of $ZrO_2$-$TiO_2$ binary oxide semiconductor nanoparticles: Application and interparticle electron transfer process, Appl. Catal. A Gen. 333 (2007) 264–271. http://doi.org/10.1016/j.apcata.2007.09.026
9. Q. Xu, M. A. Anderson, Synthesis of porosity controlled ceramic membranes, J. Mater. Res. 6 (1991) 1073–1081. http://doi.org/10.1557/JMR.1991.1073
10. G. Sun, X. Du, M. Zhang, C. Zhou, J. Chen, F. Liu, Fabrication of Zirconia Fibers by a Sol-Gel Combined Rotational Centrifugal Spinning Technique, Trans. Indian Ceram. 73 (2014) 228–232. http://doi.org/10.1080/0371750X.2014.897261

11. H. Liu, Y. Chen, S. Pei, G. Liu, J. Liu, Preparation of nanocrystalline titanium dioxide fibers using sol-gel method and centrifugal spinning, J. Solgel Sci. Technol. 65 (2013) 443–451. http://doi.org/10.1007/s10971-012-2956-7

12. H. Wang, X. Zhang, N. Wang, Y. Li, X. Feng, Y. Huang, C. Zhao, Z. Liu, M. Fang, G. OU, H. Gao, X. Li, H. Wu, Ultralight, scalable, and high-temperature–resilient ceramic nanofiber sponges, Sci. Adv. 3 (2017), e1603170. http://doi.org/10.1126/sciadv.1603170

13. D. Li, Y. Xia, Fabrication of titania nanofibers by electrospinning, Nano Lett. 3 (2003) 555–560. http://doi.org/10.1021/nl034039o

14. Y. Li, J.-H. He, Fabrication and characterization of $ZrO_2$ nanofibers by critical bubble electrospinning for high-temperature-resistant adsorption and separation, Adsorp. Sci. Technol. 37 (2019) 425–437. http://doi.org/10.1177/0263617419828268

15. Y. Zhang, S. Liu, J. Yan, X. Zhang, S. Xia, Y. Zhao, J. Yu, B. Ding, Superior Flexibility in Oxide Ceramic Crystal Nanofibers, Adv. Mater. 33 (2021), 2105011. http://doi.org/10.1002/adma.202105011

16. X. Zhang, Y. Liu, Y. Si, J. Yu, B. Ding, Flexible and tough zirconia-based nanofibrous membranes for thermal insulation, Compos. Commun. 33 (2022), 101219. https://doi.org/10.1016/j.coco.2022.101219

17. Q. Xu, M.A. Anderson, Sol–Gel Route to Synthesis of Microporous Ceramic Membranes: Thermal Stability of $TiO_2$–$ZrO_2$ Mixed Oxides, J. Am. Ceram. Soc. 76 (1993) 2093–2097. http://doi.org/10.1111/j.1151-2916.1993.tb08338.x

18. J. Dong, Y. Xie, L. Liu, Z. Deng, W. Liu, L. Zhu, X. Wang, D. Xu, G. Zhang, Lightweight and Resilient $ZrO_2$–$TiO_2$ Fiber Sponges with Layered Structure for Thermal Insulation, Adv. Eng. Mater. 24 (2022), 2101603. http://doi.org/10.1002/adem.202101603

19. M. Su, J. Wang, H. Du, P. Yao, Y. Zheng, X. Li, Characterization and humidity sensitivity of electrospun $ZrO_2$:$TiO_2$ hetero-nanofibers with double jets, Sens. Actuators B Chem. 161 (2012) 1038–1045. http://doi.org/10.1016/j.snb.2011.12.005

20. A.S. Yasin, M. Obaid, M.H. El-Newehy, S.S. Al-Deyab, N.A.M Barakat, Influence of $Ti_xZr_{(1-x)}O_2$ nanofibers composition on the photocatalytic activity toward organic pollutants degradation and water splitting, Ceram. Int. 41 (2015) 11876–11885. https://doi.org/10.1016/j.ceramint.2015.05.156.

21. G. Yu, L. Zhu, G. Zhang, G. Qin, H. Fu, F. Ji, J. Zhao, Preparation and characterization of the continuous titanium-doped $ZrO_2$ mesoporous fibers with large surface area, J. Porous Mater. 21 (2014) 105–112. http://doi.org/10.1007/s10934-013-9753-8

22. J. Song, X. Wang, J. Yan, J. Yu, G. Sun, B. Ding, Soft Zr-doped $TiO_2$ nanofibrous membranes with enhanced photocatalytic activity for water purification, Sci. Rep. 7 (2017) 1636. http://doi.org/10.1038/s41598-017-01969-w

23. N.A.M. Barakat, A.A.Y. Hassan, S.M.E.-S. Matar, M.O.A. Awad, A.S.Y. Ali, $ZrO_2$/$TiO_2$ nanofiber catalyst for effective liquefaction of agricultural wastes in subcritical methanol, Sep. Sci. Technol. 53 (2018) 2628–2638. http://doi.org/10.1080/01496395.2018.1458876

24. P. Pokorny, E. Koštáková, F. Sanetmik,P. Mikes, J. Chvojka, T. Kalous, M. Bilek, K. Pejchar, J. Valtera, D. Lukaš, Effective AC needleless and collectorless electrospinning for yarn production, Phys. Chem. Chem. Phys.16 (2014) 26816–26822. https://doi.org/10.1039/c4cp04346d

25. A.M. Drews, L. Cademartiri, G.M. Whitesides, K.J.M. Bishop, Electric winds driven by time oscillating corona discharges, J. Appl. Phys. 114 (2012), 143302. https://doi.org/10.1063/1.4824748

26. J. Valtera, T. Kalous, P. Pokorny, O. Batka, M. Bilek, J. Chvojka, P. Mikes, E. Kuzelova Kostakova, J. Spankova, J. Beran, A. Stanishevsky, D. Lukas, Fabrication of dual-functional composite yarns with a nanofibrous envelope using high throughput AC needleless and collectorless electrospinning, Sci. Rep. 9 (2019), 1801. https://doi.org/10.1038/s41598-019-38557-z

27. T. Kalous, P. Holec, R. Jirkovec, D. Lukas, J. Chvojka, Improved spinnability of PA 6 solutions using AC electrospinning, Matter. Lett. 283 (2021), 128761. https://doi.org/10.1016/j.matlet.2020.128761

28. C. Lawson, A. Stanishevsky, M. Sivan, P. Pokorny, D. Lukáš, Rapid fabrication of poly(ε-caprolactone) fibers using needleless alternating current electrospinning, J. Appl. Polym. Sci., 133 (2016), 43232. https://doi.org/10.1002/app.43232

29. R. Jirkovec, P. Holec, S. Hauzerova, A. Samkova, T. Kalous, J. Chvojka, Preparation of a composite scaffold from polycaprolactone and hydroxyapatite particles by means of alternating current electrospinning, ACS Omega 6 (2021) 9234–9242. https://doi.org/10.1021/acsomega.1c00644

30. A. Kennell, M. MacEwen, M. Armstrong, T. Nicola, B. Halloran, N. Ambalavanan, A. Stanishevsky, Fish skin gelatin nanofibrous scaffolds spun using alternating field electrospinning and *in-vitro* tested with tdTomato mice fibroblasts, Mater. Today Comm. 31 (2022), 103417. https://doi.org/10.1016/j.mtcomm.2022.103417

31. A. Stanishevsky, J. Tchernov, Mechanical and transport properties of fibrous amorphous silica meshes and membranes fabricated from compressed electrospun precursor fibers, J. Non-Cryst. Sol. 525 (2019), 119653. https://doi.org/10.1016/j.jnoncrysol.2019.119653

32. A. Stanishevsky, W.A. Brayer, P. Pokorny, T. Kalous, D. Lukáš, Nanofibrous alumina structures fabricated using high-yield alternating current electrospinning, Ceram. Int. 42 (2016) 17154–17161. https://doi.org/10.1016/j.ceramint.2016.08.003

33. A. Stanishevsky, R. Yager, J. Tomaszewska, M. Binczarski, W. Maniukiewicz, I. Witońska, D. Lukas, Structure and mechanical properties of nanofibrous $ZrO_2$ derived from alternating field electrospun precursors, Ceram. Int. 45 (2019) 18672. https://doi.org/10.1016/j.ceramint.2019.06.092

34. S. Nealy, C. Severino, A. Brayer, A. Stanishevsky, Nanofibrous $TiO_2$ produced using alternating field electrospinning of titanium alkoxide precursors: crystallization and phase development, RSC Adv. 10 (2020) 6840-6849. http://doi:10.1039/C9RA10464J

35. B. Farkas, A. Balogh, R. Cselkó, K. Molnár, A. Farkas, E. Borbás, G. Marosi, Z.K. Nagy, Corona alternating current electrospinning: A combined approach for increasing the productivity of electrospinning, Int. J. Pharm. 561 (2019) 219–227. https://doi.org/10.1016/j.ijpharm.2019.03.005

36. T. Kemmitt, M. Daglish, Decomposition of coordinated acetylacetonate in lead zirconate titanate (PZT) precursor solutions, Inorg. Chem. 37 (1998) 2063–2065. https://doi.org/10.1021/ic971131c

37. H. Preiss, E. Schierhorn, K.W. Brzezinka, Synthesis of polymeric titanium and zirconium precursors and preparation of carbide fibres and films, . Mater. Sci. 33 (1998) 4697–4706, https://doi.org/10.1023/A:1004428818457

38. B. Aramide, A. Kothandaraman, M. Edirisinghe, S.N. Jayasinghe, Y. Ventikos, General computational methodology for modeling electrohydrodynamic flows: Prediction and

optimization capability for the generation of bubbles and fibers, Langmuir 35 (2019) 10203−10212. https://doi.org/10.1021/acs.langmuir.8b03763

39. G.D. Barmparis, Z. Lodziana, N. Lopez, I.N. Remediakis, Nanoparticle shapes by using Wulff constructions and first-principles calculations, Beilstein J. Nanotechnol. 6 (2015) 361–368. https://doi.org/10.3762/bjnano.6.35
40. F. Jiang, L. Yang, D. Zhou, G. He, J. Zhou, F. Wang, Z.G. Chen, First-principles atomistic Wulff constructions for an equilibrium rutile $TiO_2$ shape modeling, Applied Surface Science, 436 (2018) 989–994. https://doi.org/10.1016/j.apsusc.2017.12.050
41. H. Näfe, D. Gautam, Metastable Nanocrystalline Zirconia in Light of the Nucleation Theory, J. Phys. Chem. C 120 (2016) 10523–10529. https://doi.org/10.1021/acs.jpcc.6b00512
42. U. Troitzsch, $TiO_2$-Doped Zirconia: Crystal Structure, Monoclinic-Tetragonal Phase Transition, and the New Tetragonal Compound $Zr_3TiO_8$, J. Am. Ceram. Soc., 89 (2006) 3201–3210. https://doi.org/10.1111/j.1551-2916.2006.01200.x
43. S. Verma, S. Rani, S. Kumar, M.A.M Khan, Rietveld refinement, micro-structural, optical and thermal parameters of zirconium titanate composites, Ceram. Int. 44 (2018) 1653–166. http://dx.doi.org/10.1016/j.ceramint.2017.10.090
44. M.J. Bannister, J.M. Barnes, Solubility of $TiO_2$ in $ZrO_2$. J. Am. Ceram. Soc. 69 (1986) C269–C271. https://doi.org/10.1111/j.1151-2916.1986.tb07373.x
45. L.M. Oanh, D.B. Do, N.M. Hung, D.V. Thang, D.T. Phuong, D.T. Ha, N.V. Minh, Formation of crystal structure of zirconium titanate $ZrTiO_4$ powders prepared by sol–gel method, J. Elec. Mater. 45 (2016) 2553–2558. https://doi.org/10.1007/s11664-016-4412-x
46. Q. Lu, D. Chen, X. Jiao, Synthesis of long $ZrTiO_4$ fibers by a sol–gel process free of organic components, J. Mater. Chem. 13 (2003) 1127–1131. https://doi.org/10.1039/b300980g

47. I.C. Cosentino, E.N.S. Muccillo, R. Muccillo, F.M. Vichi, Low-Temperature Sol-Gel Synthesis of Single-Phase $ZrTiO_4$ Nanoparticles, J. Sol-Gel Sci. Tech. 37 (2006) 31–37. https://doi.org/10.1007/s10971-005-5062-2

48. M. Sun, T. Zhao, Z. Ma, Z. Li, Facile preparation of macro-mesoporous zirconium titanate monoliths via a sol–gel reaction accompanied by phase separation, J. Mater. Res. 34 (2019) 4066–4075. https://doi.org/10.1557/jmr.2019.280

49. S.N. Koc, Zirconium titanate synthesis by diethanol amine based sol-gel route, J. Sol-Gel Sci. Techn. 38 (2006) 277–281. https://doi.org/10.1007/s10971-006-6728-0

50. E.L. Sham, M.A.G. Aranda, E.M. Farfan-Torres, J.C. Gottifredi, M. Martõnez-Lara, S. Bruque, Zirconium titanate from sol–gel synthesis: Thermal decomposition and quantitative phase analysis, J. Sol. State Chem. 139 (1998) 225–232. https://doi.org/10.1006/jssc.1998.7833

51. X. Lv, G. Yang, C. Feng, T. Lin, Highly sensitive humidity sensor based on the solid solution $Zr_{0.2}Ti_{0.8}O_2$ nanofibers, J. Alloys Comp. 891 (2021), 161958. https://doi.org/10.1016/j.jallcom.2021.161958

**Table 1.** Selected parameters of the precursor, fiber flow and resulting ceramic nanofibers

| Zr:Ti molar ratio | Precursor viscosity, mPa·s | Precursor electrical conductivity, μS/cm | Precursor flow take off rate, mL/min | Oxide nanofiber productivity, mg/min | TGA – Mass loss, % | EDS Zr/Ti molar ratio, % (1000 °C) |
|---|---|---|---|---|---|---|
| 0.9:0.1 | 122±5 | 355 | 1.10 | 80 | 52 | 87.3:12.7 |
| 0.7:0.3 | 114±5 | 200 | 1.20 | 84.4 | 46.5 | 70.7:29.3 |
| 0.5:0.5 | 117±5 | 88.6 | 1.43 | 100.5 | 54 | 50.8:49.2 |
| 0.2:0.8 | 120±5 | 19.9 | 1.55 | 107 | 46 | 18.9:81.1 |

**FIGURE CAPTIONS**

**Figure 1.** (a) Mass loss and (b) DTA signals during TGA of $Zr_xTi_{1-x}O_2$ nanofibers with 0.9:0.1, 0.7:0.3, 0.5:0.5 and 0.2:0.8 Zr/Ti molar ratios. The insets show the expanded regions of interest. (c) Positive ion emission during TGA of the fibers with 0.7:0.3 Zr/Ti molar ratio.

**Figure 2.** (a-d) SEM images and (e-h) Energy dispersive X-ray spectra (EDS) of $Zr_xTi_{1-x}O_2$ nanofibers with 0.9:0.1, 0.7:0.3, 0.5:0.5 and 0.2:0.8 Zr/Ti molar ratios, respectively, after calcination at 600 °C.

**Figure 3.** Trends in the average fiber diameter change with the annealing temperature for $Zr_xTi_{1-x}O_2$ nanofibers with different compositions. Dotted lines are to guide the viewer's eye.

**Figure 4.** Characteristic SEM images of $Zr_xTi_{1-x}O_2$ nanofibers with (a,e,i) 0.9:0.1, (b,f,j) 0.7:0.3, (c,g,k) 0.5:0.5 and (d,h,l) 0.2:0.8 Zr/Ti molar ratios, respectively, after thermal processing at (a-d) 800 °C, (e-h) 1000 °C, and (i-l) 1200 °C.

**Figure 5.** XRD patterns of $ZrO_2$:$TiO_2$ nanofibers with (a) 0.9:0.1, (b) 0.7:0.3, (c) 0.5:0.5 and (d) 0.2:0.8 Zr/Ti molar ratios, respectively, after thermal processing at different temperatures. Symbols ○ indicate major peaks of t-$ZrO_2$ phase, ● – m-$ZrO_2$, ▼ – possible $Zr_3TiO_8$, ◊ – $Zr_{0.5}Ti_{0.5}O_2$, ▫ – $TiO_2$ anatase, ▪ – $TiO_2$ rutile, Δ – $Zr_{0.33}Ti_{0.67}O_2$, and × – $Zr_{0.45}Ti_{0.55}O_2$.

**Figure 6.** (a-c) Trends in the average crystallite size change with the annealing temperature for $Zr_xTi_{1-x}O_2$ nanofibers with different compositions. Dotted lines are to guide the viewer's eye.

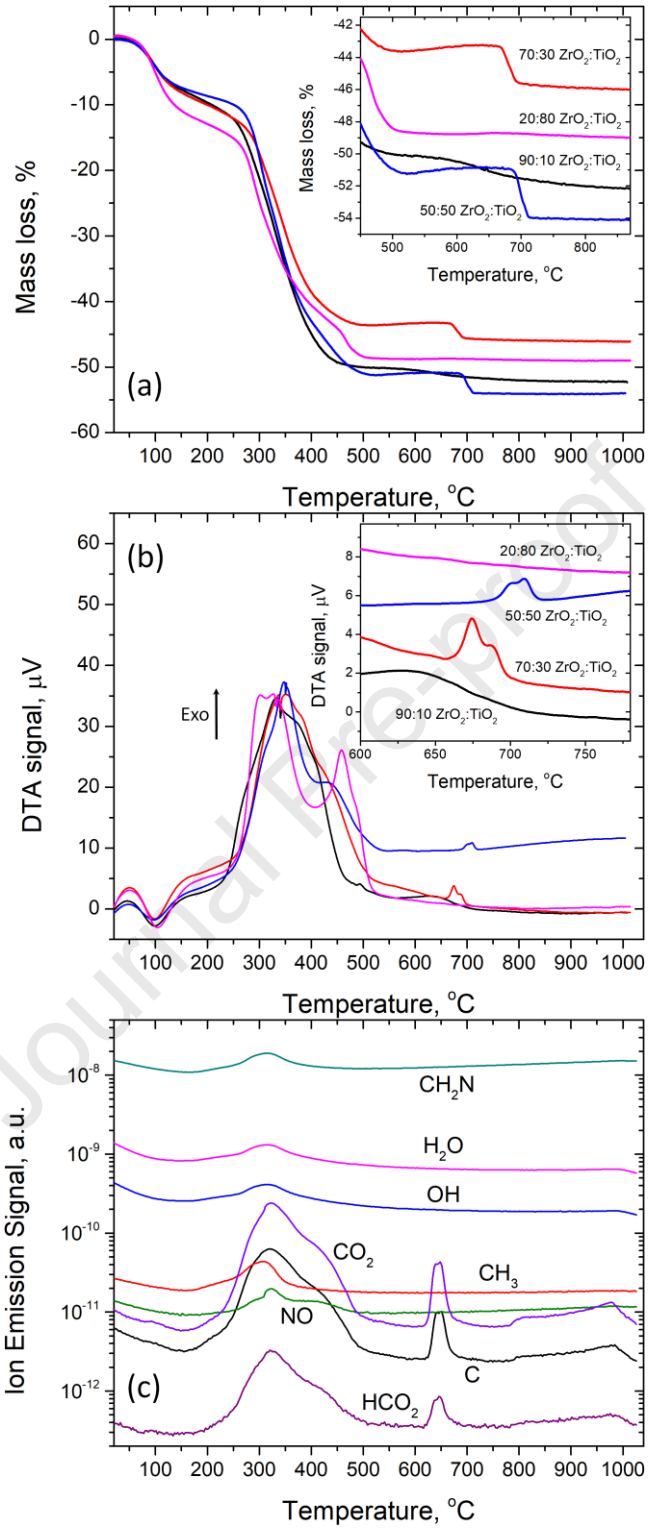


**Figure 1.** (a) Mass loss and (b) DTA signals during TGA of $Zr_xTi_{1-x}O_2$ nanofibers with 0.9:0.1, 0.7:0.3, 0.5:0.5 and 0.2:0.8 Zr/Ti molar ratios. The insets show the expanded regions of interest. (c) Positive ion emission during TGA of the fibers with 0.7:0.3 Zr/Ti molar ratio.

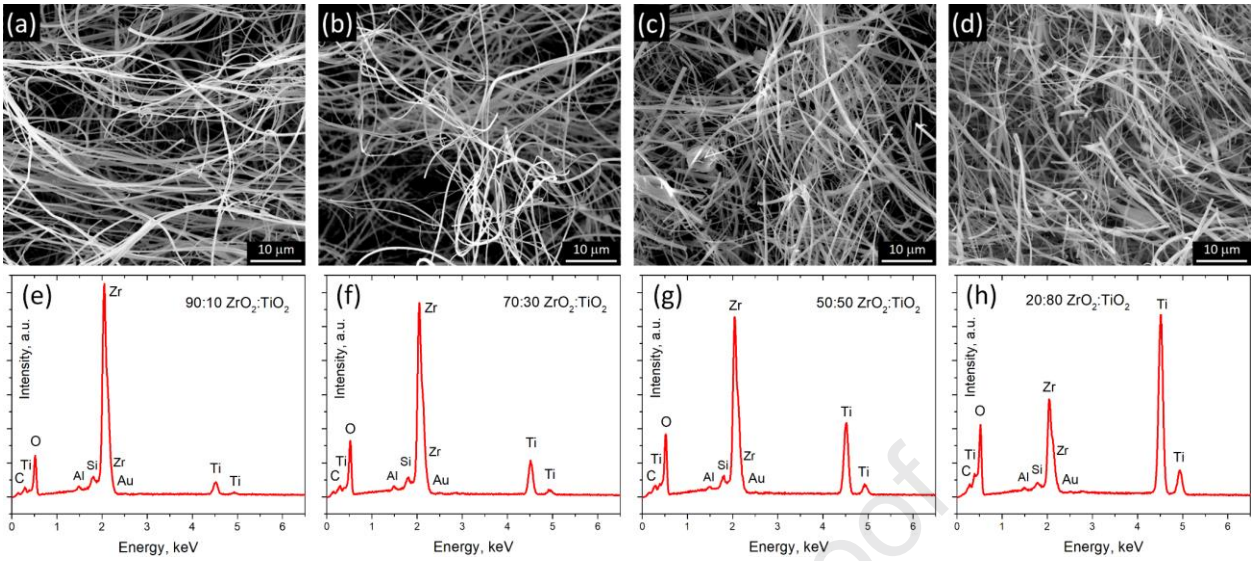


**Figure 2.** (a-d) SEM images and (e-h) Energy dispersive X-ray spectra (EDS) of $Zr_xTi_{1-x}O_2$ nanofibers with 0.9:0.1, 0.7:0.3, 0.5:0.5 and 0.2:0.8 molar ratios, respectively, after calcination at 600 °C.

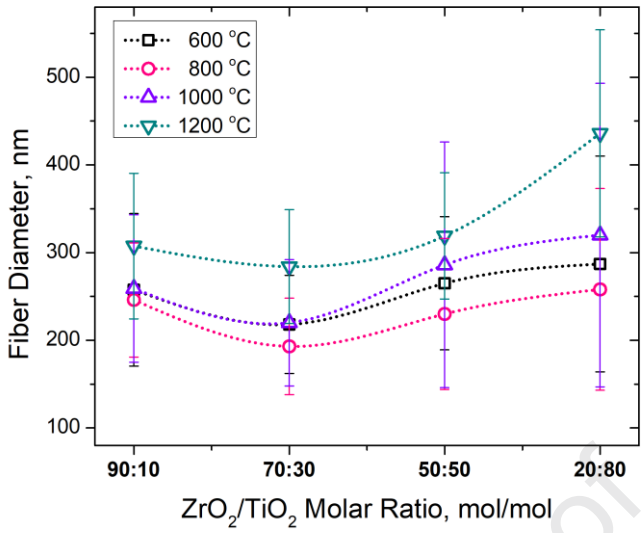


**Figure 3.** Trends in the average fiber diameter change with the annealing temperature for $Zr_xTi_{1-x}O_2$ nanofibers with different compositions. Dotted lines are to guide the viewer's eye.

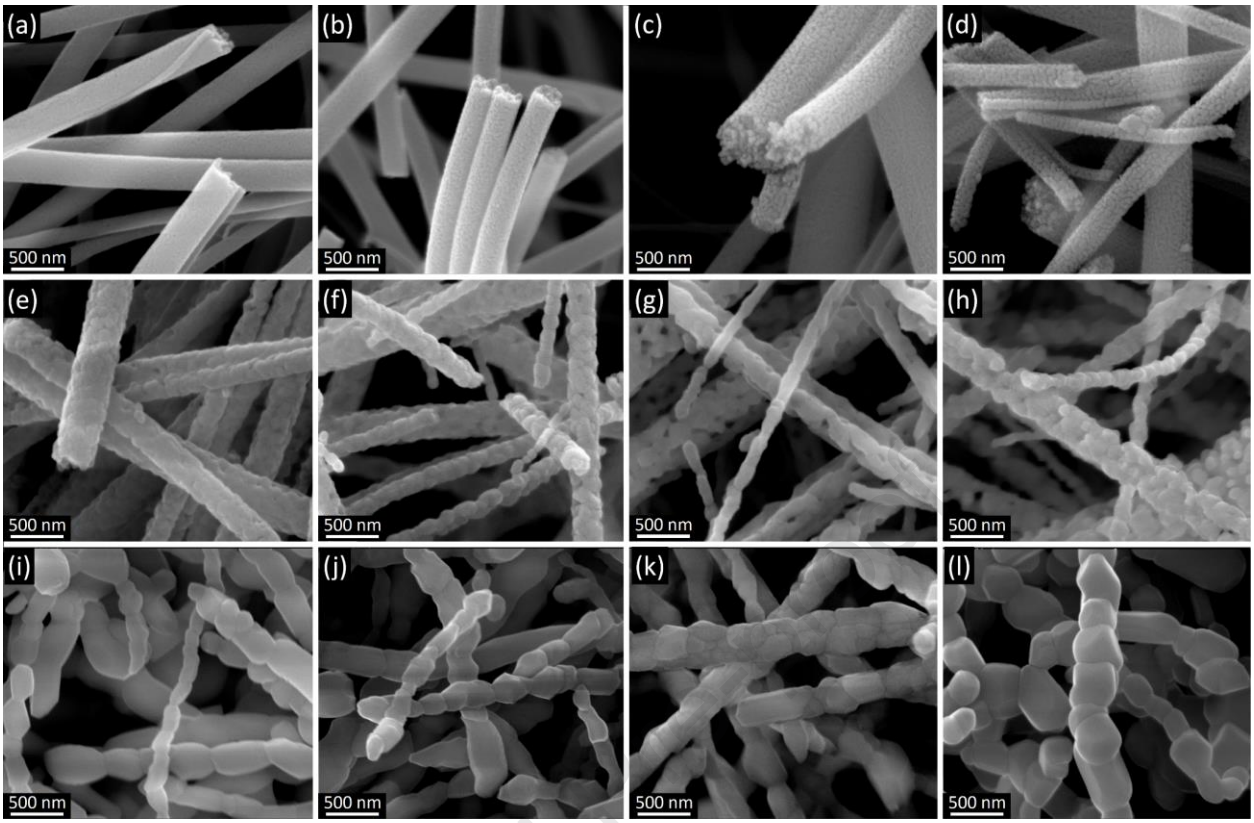


**Figure 4.** Characteristic SEM images of $Zr_xTi_{1-x}O_2$ nanofibers with (a,e,i) 0.9:0.1, (b,f,j) 0.7:0.3, (c,g,k) 0.5:0.5 and (d,h,l) 0.2:0.8 Zr/Ti molar ratios, respectively, after thermal processing at (a-d) 800 °C, (e-h) 1000 °C, and (i-l) 1200 °C.

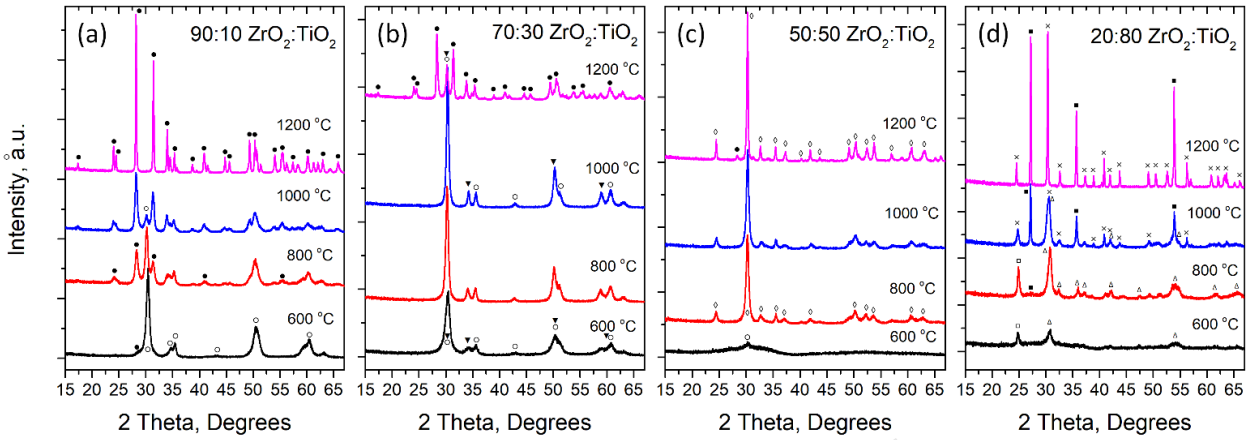


**Figure 5.** XRD patterns of $ZrO_2$:$TiO_2$ nanofibers with (a) 0.9:0.1, (b) 0.7:0.3, (c) 0.5:0.5 and (d) 0.2:0.8 Zr/Ti molar ratios, respectively, after thermal processing at different temperatures. Symbols ○ indicate major peaks of t-$ZrO_2$ phase, ● – m-$ZrO_2$, ▼ – possible $Zr_3TiO_8$, ◊ – $Zr_{0.5}Ti_{0.5}O_2$, □ – $TiO_2$ anatase, ■ – $TiO_2$ rutile, Δ – $Zr_{0.33}Ti_{0.67}O_2$, and × – $Zr_{0.45}Ti_{0.55}O_2$.

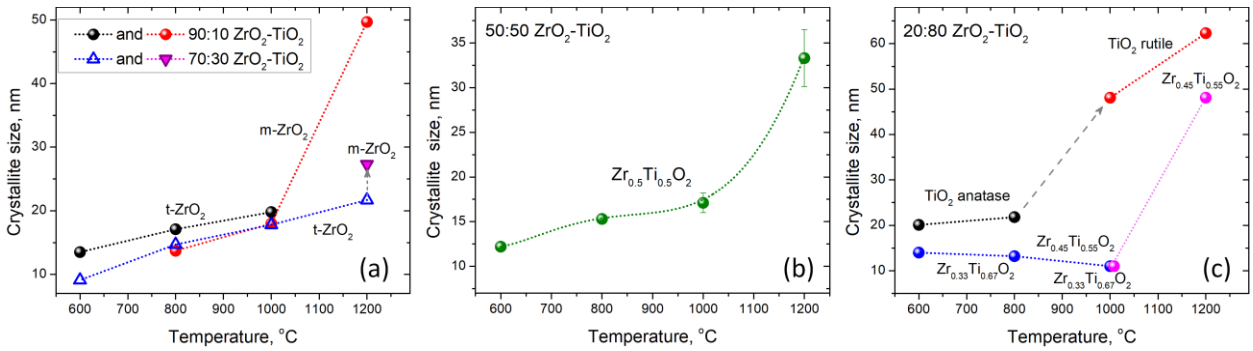


**Figure 6.** (a-c) Trends in the average crystallite size change with the annealing temperature for $Zr_xTi_{1-x}O_2$ nanofibers with different compositions. Dotted lines are to guide the viewer's eye.

**Table 1.** Selected parameters of the precursor, fiber flow and resulting ceramic nanofibers

| Zr:Ti molar ratio | Precursor viscosity, mPa·s | Precursor electrical conductivity, μS/cm | Precursor flow take off rate, mL/min | Oxide nanofiber productivity, mg/min | TGA – Mass loss, % | EDS Zr/Ti molar ratio, % (1000 °C) |
|---|---|---|---|---|---|---|
| 0.9:0.1 | 122±5 | 355 | 1.10 | 80 | 52 | 87.3:12.7 |
| 0.7:0.3 | 114±5 | 200 | 1.20 | 84.4 | 46.5 | 70.7:29.3 |
| 0.5:0.5 | 117±5 | 88.6 | 1.43 | 100.5 | 54 | 50.8:49.2 |
| 0.2:0.8 | 120±5 | 19.9 | 1.55 | 107 | 46 | 18.9:81.1 |